physica status solidi a
www.pss-a.com

Epitaxial Lateral Overgrowth of Wafer-Scale Heteroepitaxial Diamond for Quantum Applications

Vadim Lebedev, Jan Engels, Tingpeng Luo, Jan Kustermann, Jürgen Weippert, Christian Giese, Lutz Kirste, Patricia Quellmalz, Jan Jeske, Volker Cimalla, and Peter Knittel*

Wafer-scale heteroepitaxial diamond thin films demonstrate multiple advantages for a further development of integrated optical and quantum devices based on impurity–vacancy color centers. The main obstacle here is a high structural defect density characteristic for heteroepitaxial epilayers. In this work, technological methods of stress control, NV formation, and defect density reduction in diamond epilayers, which are based on principles of epitaxial lateral overgrowth (ELO) are reported on. Herein, material and quantum properties of NV-doped diamond thin films obtained by patterned nucleation growth and by ELO of microstructured epilayers, are compared. It is demonstrated that a combination of both methods might have a significant potential for the wafer-scale production of heteroepitaxial diamond for quantum devices.

1. Introduction

Wafer-scale heteroepitaxial diamond (HD) thin films grown by plasma-assisted chemical vapor deposition (CVD) on iridium (Ir) substrates via bias-enhanced nucleation (BEN) demonstrate multiple advantages for an actual development and for commercialization of integrated optical and quantum devices based on impurity–vacancy color centers (NV, SiV, GeV, etc.).[1,2] One of the main obstacles on this route is a high structural defect density of $N_D \approx 10^7$–$10^9\,cm^{-2}$ characteristic for HD epilayers.[3] In comparison, the CVD films grown homoepitaxially on high-pressure high-temperature (HPHT) diamond platelets demonstrate N_D of $\approx 10^4\,cm^{-2}$, sufficient for a performance currently requested for optical and quantum sensors. The homoepitaxial approach is, however, severely limited by the HPHT substrates' size of $\approx 10 \times 10\,mm^2$ originating from the growth conditions. On the contrary, free-standing HD specimen with a diameter up to 90 mm and with a defect density of $<10^7\,cm^{-2}$ has already been demonstrated.[4]

In this work, we analyze two technological methods of N_D reduction in wafer-scale HD, which are based on principles of epitaxial lateral overgrowth (ELO). Here, we compare NV-doped HD samples obtained by 1) patterned nucleation growth (PNG, type I)[5] and 2) overgrowth of microstructured heterodiamond epilayers (type II). In particular, N(P1) and NV densities, along with a dephasing time T_2*, have been experimentally obtained and compared to those measured on homoepitaxial reference samples.[6] In addition, potential advantages of secondary BEN/CVD processing on Ir-on-diamond substrates (type III) are briefly discussed and the crystal quality of epilayers of different types is compared. In addition to quantum performance parameters, the results on microstructural and optical characterization of HD epilayers are reported highlighting the advances of ELO in achieving a "quantum grade" for diamond thin films on a wafer scale.

2. Experimental Section

2.1. Type I Sample Preparation

Thin nitrogen-doped HD (001) films are nucleated and grown in a 2.45 GHz, 1.5 kW plasma-assisted BEN/CVD reactor (CVD1 in SDS6200 by Seki Diamond/Cornes Technologies) on 120 nm thick Ir epilayers. Ir(100) is grown on ∅50 mm nominally on-axis 1 mm thick Si(100) substrates using an yttria-stabilized zirconia epilayer by means of a high-temperature sputter deposition technique (CLN200 by Evatec). Long-term deposition (CVD2) is carried out in ellipsoidal plasma reactors up to an epilayer thickness of 200–300 µm. **Figure 1**e shows schematically the fabrication steps employed for HD sample production including BEN (A), BEN patterning (B), and CVD-ELO (C) stages. The BEN and CVD growth parameters are summarized in **Table 1**. Additional details on the sputter and CVD equipment along with a description of the technological procedures can be found elsewhere.[7–9]

All HD films are deposited using a [100] preferential growth mode ($\alpha \rightarrow 3$).[3] In this particular case, a growth rate (R_{hkl})

V. Lebedev, J. Engels, T. Luo, J. Kustermann, J. Weippert, C. Giese, L. Kirste, P. Quellmalz, J. Jeske, V. Cimalla, P. Knittel
Fraunhofer Institute for Applied Solid State Physics, IAF
Tullastraße 72, 79108 Freiburg, Germany
E-mail: vadim.lebedev@iaf.fraunhofer.de

The ORCID identification number(s) for the author(s) of this article can be found under https://doi.org/10.1002/pssa.202300325.

DOI: 10.1002/pssa.202300325

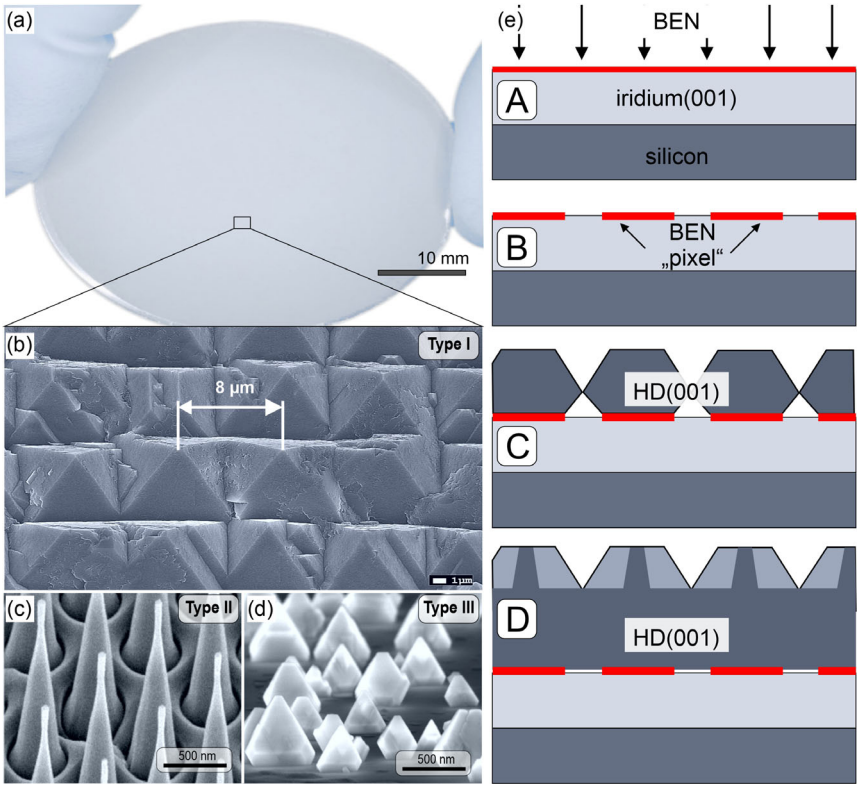

Figure 1. a) Photograph and b) SEM micrograph taken on a 10–15 µm thick HD layer grown using the ELO-PNG technique with a PNG pitch of 8 µm (45° view); c,d) SEM micrographs of (c) a type II microstructured sample with a 2D pillar array having pitch of 1 µm (45° view), and (d) a type III sample surface after the secondary BEN/CVD has been carried out on polished Ir_on_HD wafer (85° view). e) Schematical representation of fabrication steps for type I and II samples: (A) BEN of Ir(001) wafers, (B) definition of ELO pattern by lithography and RIE, (C) ELO of type I samples (CVD1 and CVD2), and (D) patterning and overgrowth of type II samples.

Table 1. HD BEN and growth conditions.

Process	Sample type	Temperature [°C]	BEN bias [V]	Pressure [Torr]	CH_4 in H_2 [%]	N_2 [ppm]	Thickness [µm]
BEN	I, III	750	400	17	5.0	–	0
CVD1	I, III	950	–	40	1.0	40	0.5–1.0
CVD2	I, II, III	830	–	120	1,75	3000	≥100

anisotropy leads to a characteristic tetragonal shape of isolated diamond microcrystals at the first stage of CVD. Due to a specific in-plane arrangement of the nuclei spots (pixels) in type I samples (see Figure 1a,b), an effective compensation of the residual stress in the grown heteroepitaxial stack might be achieved.[5]

At the later stage of the growth, the isolated microcrystals undergo a coalescence forming a closed HD epilayer. The thickness for such HD films might range from 20 to 200 µm, depending on the growth conditions and crystal quality requirements.

2.2. Type II and III Sample Preparation

As-grown type I HD wafers are mechanically polished down to a surface roughness of $R_q \approx 2$ nm. Type II samples are fabricated on polished type I PNG templates using electron-beam lithography and reactive ion etching (RIE) followed by overgrowth of micromachined periodic structures using the CVD2 process parameters. In Figure 1c, an example of type II template surface is displayed showing a microstructured HD surface filled with a high-aspect ratio "pillar" array. Figure 1e schematically (stage D) shows a cross section of overgrown type II sample. Further details on RIE and related pattering procedures can be found elsewhere.[6]

Further processing of type I HD wafers using mechanical planarization/polishing processes, followed by the removal of the silicon substrates and by Ir sputter epitaxy, allows for the fabrication of very high-quality Ir layers. Ir_on_HD samples have a low initial stress and ensure a high-density BEN/CVD of HD microcrystals with a dramatically improved orientation grade of isolated microcrystals (type III, see Figure 1d). With a typical BEN density of $>10^{11}$ cm^{-2} and an orientation grade of >90%, this method allows growing thin functional HD layers of high quality on a metallic layer, which can be used either as a sacrificial layer, electrode, or optical mirror in quantum and optoelectronic devices.

2.3. Characterization

All prepared HD samples are characterized using scanning electron microscopy (SEM), high-resolution X-ray diffraction (HRXRD) along with Raman, cathodoluminescence (CL), and photoluminescence (PL) spectroscopy. As the crystal quality of HD rises gradually with the thickness, XRD measurements are strongly affected by a lower quality nucleation layer. The best value of full width at half maximum (FWHM) for the 004 reflection of 0.14° is measured on a 220 µm thick, as-grown (001) HD film.

Raman and PL spectra are measured using a Renishaw InVia Raman microscope in which a 532 nm laser excites the NV centers and the integrated NV response signal is detected. The PL and Raman measurements are carried out at excitation laser powers of <0.1 µW and 1.0 mW, respectively. During PL measurements, the laser focus is set inside the HD epilayer in the proximity of heterointerface. CL measurements are carried out in a Jeol JSM-7610F SEM equipped with built-in CL system manufactured by Gatan. Optically detected magnetic resonance (ODMR) measurements are carried out using a home-built confocal setup. More detailed information on ODMR and T_2* measurements can be found elsewhere.[6,10]

3. Results and Discussion

3.1. Growth and Properties of Type I HD Epilayers

As mentioned in the previous section, type I PNG films are deposited using an α→3 growth mode resulting in a tetragonal shape of isolated diamond microcrystals (pixels, see Figure 1b). The advantage of such artificially defined pixel structures is the possibility to control radial and tangential stress distributions by varying pitch and in-plane arrangement of the pixels. On the other hand, a long-term CVD on such ordered pyramid arrays results in the formation of additional grain boundaries (GBs) causing unwanted undulation of the NV emission properties. In **Figure 2**, this particular phenomenon is illustrated by a comparison of the SEM image of a thick type I HD epilayer (Figure 2a) and a corresponding PL map representing integrated light emission from NV ensembles (centered around zero-phonon line of NV-ZPL at 638 nm) (Figure 2b). Despite a restricted spatial resolution of the PL setup (≈200 nm with 100× NA = 0.5 objective), one can recognize much lower NV-related emission from the GB areas. Here, three possible reasons might be considered: 1) ray-optic phenomena such as multireflection and light trapping, 2) high broadband absorption (i.e., due to sp^2 inclusions), and 3) lower density of properly formed impurity–vacancy spatial configurations, e.g., due to high ND and lattice disorder.

More detailed information can be obtained using high-resolution CL studies by comparing spectral features of CL signals measured at a "high-quality" area showing maximal NV signal and at GB (Figure 2c). First, it is important to mention that the CL peak related to the free excitons (X_{TO}) is clearly observable, indicating a high crystal lattice quality of the analyzed HD samples. The obvious differences in the two spectra in Figure 2c are the pronounced "green" and "blue" regions (the so-called A-band) of the CL curve taken at GB. A-band are usually

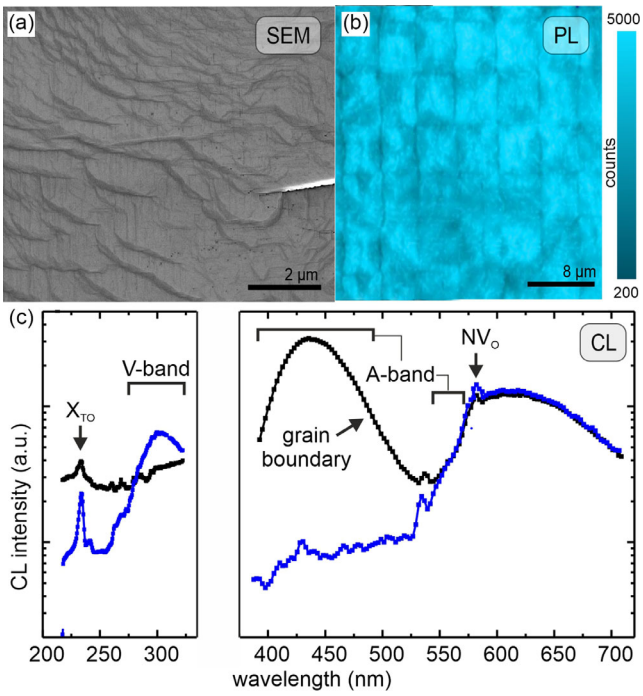

Figure 2. a) SEM micrograph taken on a 100 µm thick type I HD epilayer along with b) an integrated PL intensity map (a.u.) measured around the NV-ZPL at 635 nm on the same sample; c) CL spectra measured at the domain center (blue curve) and at the vicinity of the GB (black curve).

associated with various lattice defects in diamond. In particular, a strong "blue" spectral region centered around 2.8 eV is associated with "close" D–A pairs.[11,12] In addition, among other possible origins for the "blue" peak, a vibronic band of dislocation-related centers and sp^2 inclusions should be also mentioned.[13,14] Therefore, according to our CL analysis and available literature data, all aforementioned mechanisms might be responsible for damping of the NV emission in GB regions in thin HD films. For thicker epilayers (>50 µm), the sp^2-related features (e.g., G-band) are not detected by Raman spectroscopy. Here, residual dislocation and point defect networks along with persistent low-angle domain boundaries can be called the main source for the NV emission damping. The observed spectral features correlate well with our previous microstructural studies,[3] where the ½<110>|(100) edge-type threading dislocations (TDs) trapped at low-angle GB were found to be the main reason for a high density of growth defects in HD epilayers.

At the later stages of CVD, for epilayer thicknesses over 200 µm, the N_D is gradually reduced down to ≈10^7 cm^{-2} via various termination mechanisms. The material parameters for a typical PNG wafer used in this work are a nitrogen dopant density of $P_1 \approx 1.8$ ppm and NV density of ≈0.3 ppb as revealed by UV/vis and PL spectrometry, respectively. The reference homoepitaxial samples show quite similar values. Pulsed ODMR measurements reveal T_2* of ≈0.32 µs on such HD epilayers, indicating that the films have a high crystal quality supporting proper formation of the NV pairs in the host lattice. Moreover, as revealed by Raman spectroscopy, an FWHM of the sp^3 peak at 1332 cm^{-1} measured on thick type I

epilayers is typically $<3\ cm^{-1}$ approaching homoepitaxial values. However, comparing HD value to T_2^* of $\geq 0.4\ \mu s$ measured on the homoepitaxial samples, we can conclude that the residual value of N_D is quite persistently reducing the NV-coherence time in HD epilayers. Therefore, additional technological methods should be employed for further improvements of NV properties and for effective reduction of N_D. In the next section, we show how CVD on a 3D-profiled HD surfaces (type II samples) affects properties of NV-doped HD epilayers.

3.2. Properties of Type II HD Epilayers

Type II HD samples are fabricated on mechanically polished type I HD wafers using conventional micromachined methods such as e-beam lithography and RIE. Optimized RIE processing results in a highly controllable shape of the isolated 3D microstructures (e.g., pillars and squared mesas, see Figure 1c), which are used as individual nucleation sites for the second ELO CVD process. Here, the main difference with a PNG CVD (type I) are the growth conditions for a diamond crystallization. NV-doped HD film grows on the 3D microstructures as well as on the planar HD surface between them. Therefore, the surface morphology might be controlled by growth conditions as well as by means of a pattern geometry, e.g., by aspect ratio and by pitch of the pillar arrays. This phenomenon is illustrated in **Figure 3**a by SEM micrographs displaying surface morphologies of HD films fabricated using the CVD overgrowth of arrays with large (flat layer, field A) and small (high-index facets, field B) cross-sectional area pillars. For type II samples, however, the most intriguing objects are isolated, high-aspect ratio pillars (Figure 3b), which can be transformed by the overgrowth into 3D objects bounded by the {111} facets. Such truncated square pyramid bounded by a top (001) and four {111} family facets is shown in Figure 3c.[15]

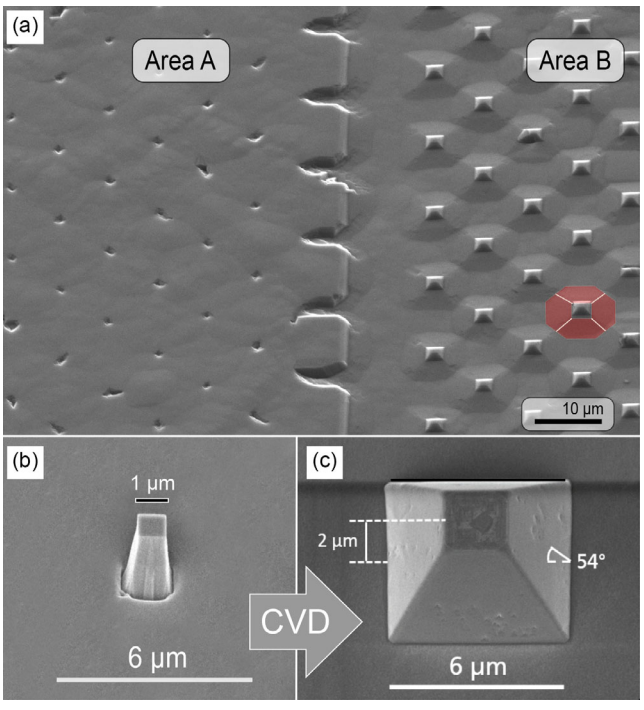

Figure 3. SEM micrographs of a) overgrown type II surface showing two neighboring regions filled with large (A) and small (B) area pillars; b) single pillar structure defined on the type II surface by RIE; and c) the same structure converted into a truncated square pyramid by ELO processing.

Basic type II epilayer parameters (i.e., P_1 and NV densities) do not differ significantly from those obtained on type I samples. On the other hand, the {111}-bounded pyramidal structures demonstrate an exceptional signal contrast in continuous wave (cw) ODMR measurements, indicating a very high grade of NV-pair alignment (>90%) on each of {111} facets. Detailed analysis of the cw ODMR results will be published elsewhere.[16] Here, we highlight that a cross-sectional PL map (**Figure 4**a) shows a characteristic spatial distribution of the NV emission within the pyramids: the most intensive signal is detected on the {111} facets, which provide advanced conditions for NV formation. In contrast, the areas corresponding to a low-doped core and a conventional (100) epilayer generate a much lower signal. Comparing these results with the previous studies carried out on homoepitaxial films,[6] we might assume that during crystallization in <111> direction in a so-called "step-flow-growth" mode, a nearly uniform alignment of NVs is achieved on each {111} facet, where each NV orientation corresponds to one of four possible orientations of the NV pair in the diamond sp^3 lattice.[17]

It is also important to mention that ODMR reveals a quite low coherence time T_2^* of $\approx 0.1\ \mu s$ on these {111}-bound pyramids. It might relate to the microstructural properties of the overgrown NV-doped film. In particular, T_2^* can be constrained by the development of an extended dislocation networks. It might be the prolonged defects propagating from the substrate or dislocations generated at an imperfect HD/HD interface. This hypothesis is schematically illustrated in Figure 4a: the dashed yellow lines show stacking faults (SFs) in <111> direction and $b = \frac{1}{2}<110>|(001)$ edge-type TDs typically generated at diamond hetero- and homointerfaces. As shown in Figure 4b, at the initial growth phase of type I pyramids, a high-density SF network is formed due to an initial lattice mismatch. Each additional interface might multiply the number of prolonged defects including SFs. In Figure 4c, this phenomenon is illustrated by the bright-field transmission microscopy image (BF TEM) of the overgrown pyramid. In addition to the denser SF network, a new network of $b = \frac{1}{2}<110>|(001)$ TDs is formed on top of the pyramid. Moreover, in type II samples, the laterally grown "wings" remain attached to the HD substrate inheriting its prolonged defects.

Hence, a total defect density in type II HD is a sum of contributions from all aforementioned sources, and it is higher comparing to the type I HD. Low T_2^* time, in this case, reflects a much higher N_D value. Additional information on quantum and optical properties of various Type II structures can be found elsewhere.[18]

4. Prospects of Type III Epilayers and Conclusions

In previous sections we have demonstrated that using ELO technique, high-quality type I HD can be nucleated by BEN and grown by CVD on a chemically inert Ir substrates. We showed that in type I HD epilayers, sufficiently high NV-coherence times

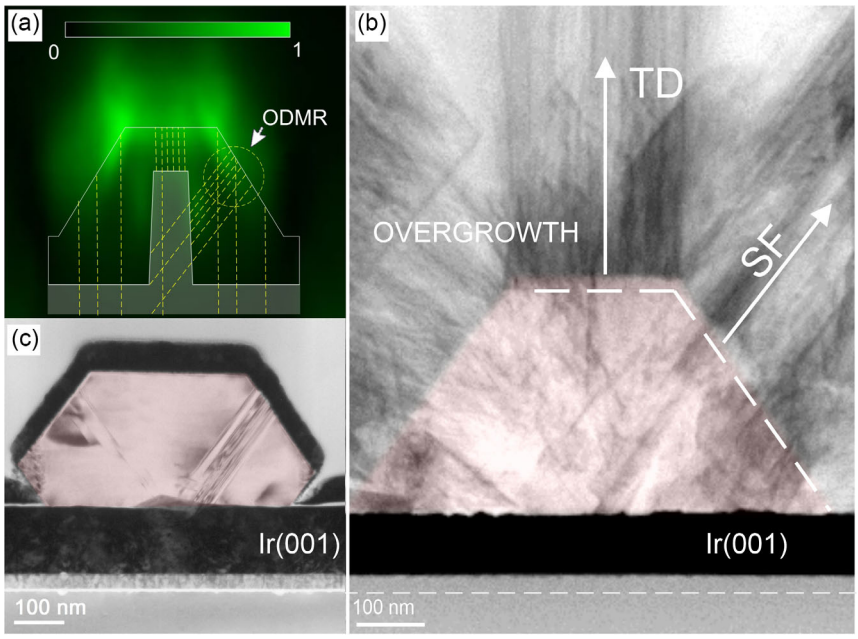

Figure 4. a) Cross-sectional PL map measured on a type II squared pyramid (shown in Figure 3c) together with a schematic representation of a dislocation network characteristic for HD epilayers; b,c) BF TEM micrographs displaying development of dislocation networks in (b) "overgrown" and (c) "not overgrown" pyramidal grains fabricated by BEN/CVD on Ir epilayers (grain areas marked by the red color).

($T_2^* \approx 0.32\,\mu s$) can be achieved, and such epilayers might be employed for the development of integrated quantum–optical or optical chips for rapid data processing. At the same time, type II microstructured HD samples show many advantages in terms of controlled surface morphology along with preferential location and spatial alignment of the NV pairs. These parameters are of a great importance for quantum sensors and integrated components for quantum computing (e.g., memory cells and registers). Both technological approaches, with their own advantages and disadvantages, might be combined into one comprehensive technological solution, which allows to achieve a "quantum grade" mark for HD on a wafer scale for sufficiently thin epilayers.

Example of such technology is shown in **Figure 5**. Here, the 2nd HD epilayer is deposited using conventional BEN/CVD technique on an Ir/HD/Ir substrate fabricated from the type I wafer. As shown in Figure 1d and 5, an Ir deposition on a fine polished HD wafer improves the results of the second CVD processing in terms of the nucleation density and orientation. Another important factor for the improvements is the absence of the thermal mismatch between the substrate (HD_1) and the epilayer (HD_2). Due to refined microstructure of the 2nd Ir film, type III samples show the nucleation density $>>10^{11}$ cm^{-2} with a nucleus orientation consistency over 95%. Consequently, thin, closed type III HD layers of high crystal quality can be nucleated and grown on the 2nd Ir layer, even without use of the 2nd PNG mask. Moreover, the first and the second HD films can be separated using femto-seconds-laser technique if their thickness exceeds 100–150 µm. The main bottlenecks for this type of technology are the grinding (planarization) and the fine polishing procedures, which are challenging for wafer-scale HD films due to a residual wafer bow and an extraordinal mechanical hardness of diamond.

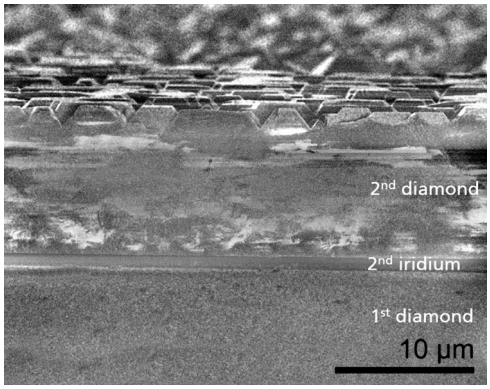

Figure 5. Cross-sectional SEM micrograph of type III HD sample displaying the second Ir and HD epilayers fabricated on a polished type I HD wafer.

Acknowledgements

The authors would like to thank M. Ardner for technical support, A. Graff for TEM studies as well as M. Prescher and N. Brückner for expert assistance for the HRXRD analyses. Funding under the GroDiaQ project of the German Federal Ministry of Education and Research (BMBF) is gratefully acknowledged.

Open access funding enabled and organized by Project DEAL.

Conflict of Interest

The authors declare no conflict of interest.

Data Availability Statement

The data that support the findings of this study are available from the corresponding author upon reasonable request.

Keywords

defects, diamond, epitaxial lateral overgrowth, heteroepitaxy, NV, optically detected magnetic resonance, quantum

Received: April 26, 2023
Revised: October 10, 2023
Published online: April 14, 2024

[1] J. Wrachtrup, F. Jelezko, *J. Phys.: Condens. Matter* **2006**, *18*, 807.
[2] R. Nelz, J. Görlitz, D. Herrmann, A. Slablab, M. Challier, M. Radtke, M. Fischer, S. Gsell, M. Schreck, C. Becher, E. Neu, *APL Mater.* **2019**, *7*, 011108.
[3] V. Lebedev, J. Engels, J. Kustermann, J. Weippert, V. Cimalla, L. Kirste, C. Giese, P. Quellmalz, A. Graff, F. Meyer, M. Höfer, V. Sittinger, *J. Appl. Phys.* **2021**, *129*, 165301.
[4] M. Schreck, S. Gsell, R. Brescia, M. Fischer, *Sci. Rep.* **2017**, *7*, 44462.
[5] T. Yoshikawa, H. Kodama, S. Kono, K. Suzuki, A. Sawabe, *Thin Solid Films* **2015**, *594*, 120.
[6] A. Götze, N. Striegler, A. Marshall, P. Neumann, C. Giese, P. Quellmalz, P. Knittel, *Phys. Status Solidi RRL* **2022**, *16*, 2100373.
[7] J. Weippert, P. Reinke, F. Benkhelifa, H. Czap, C. Giese, L. Kirste, P. Straňák, J. Kustermann, J. Engels, V. Lebedev, *Crystals* **2022**, *12*, 1626.
[8] V. Lebedev, T. Yoshikawa, C. Giese, L. Kirste, A. Žukauskaitė, A. Graff, F. Meyer, F. Burmeister, O. Ambacher, *J. Appl. Phys.* **2019**, *125*, 075305.
[9] T. Yoshikawa, D. Herrling, F. Meyer, F. Burmeister, C. E. Nebel, O. Ambacher, V. Lebedev, *J. Vac. Sci. Technol., B* **2019**, *37*, 021207.
[10] T. Luo, L. Lindner, J. Langer, V. Cimalla, X. Vidal, F. A. Hahl, C. Schreyvogel, S. Onoda, S. Ishii, T. Ohshima, D. Wang, D. A. Simpson, B. C. Johnson, M. Capelli, R. Blinder, J. Jeske, *New J. Phys.* **2022**, *24*, 033030.
[11] A. T. Collins, *Diamond Relat. Mater.* **1992**, *1*, 457.
[12] R. J. Graham, T. D. Moustakas, M. M. Disko, *J. Appl. Phys.* **1991**, *69*, 3212.
[13] K. Iakoubovskii, G. J. Adriaenssens, *Phys. Rev. B* **2000**, *61*, 10174.
[14] D. Takeuchi, H. Watanabe, S. Yamanaka, H. Okushi, H. Sawada, H. Ichinose, T. Sekiguchi, K. Kajimura, *Phys. Rev. B* **2001**, *63*, 245328.
[15] A. Götze, *Doctoral Thesis*, University of Freiburg (Germany), **2022**.
[16] J. Engels, J. Weippert, P. Quellmalz, C. Giese, T. Luo, N. Mathes, L. Lindner, J. Jeske, P. Knittel, L. Kirste, J. Kustermann, V. Lebedev, **2023**, submitted.
[17] L. M. Pham, N. Bar-Gill, D. Le Sage, C. Belthangady, A. Stacey, M. L. Markham, D. J. Twitchen, M. D. Lukin, R. L. Walsworth, *Phys. Rev. B* **2012**, *86*, 121202.
[18] J. Weippert, J. Engels, P. Quellmalz, C. Giese, T. Luo, N. Mathes, L. Lindner, J. Jeske, P. Knittel, L. Kirste, J. Kustermann, V. Lebedev, *J. Appl. Phys.* **2023**, *133*, 234401.